SUPPLEMENTAL METHODS:

Animal Monitoring

The animals were monitored throughout the study using a veterinary multi-parameter monitor (SurgiVet V9212AR (2006)) to ensure stable hemodynamics during imaging. The monitor measures heart rate and tracks the heart's electrical activity via a 3 lead electrocardiogram. It also measures respiratory rate, oxygen saturation, end-tidal carbon dioxide levels and blood pressure. Diastolic (DBP) and systolic blood pressures (SBP) were obtained using a pressure cuff placed around the animal's front limb. A summary of the blood pressures and heart rates is given in Supplemental Table 1. The SBPs were consistent with that seen in this model by others (12). The DBPs were stable throughout the imaging sessions but observed to be lower than expected suggesting a possible underestimation of BP in these experiments.

Camera

The camera used in this study was the Discovery NM 530c (GE Healthcare). This camera is a dedicated cardiac camera that uses 19 cadmium-zinc-telluride (CZT) based detectors (*14*). Each detector is 8 x 8 cm divided into a 32x32 array with a pixel pitch of 2.46 mm. Each detector has a single-pinhole collimator with an effective diameter of 5.1 mm. The detectors are arranged in an arc around the field-of-view, providing sufficient angular sampling for 3D reconstruction without the need to rotate the camera. The sensitivity of the system is approximately 4-times higher than a standard dual-head gamma camera (*14*). The dead-time of the system is negligible up to its maximum count rate of ~600 kcps (*14*) allowing reliable acquisition at the very high count rates that occur immediately following tracer injection.

Image Reconstruction

Projection data for each time frame were independently reconstructed using manufacturer supplied generalized EM-MAP iterative reconstruction that included point-spread function modeling and a noise-

suppression prior (*14*). Thirty iterations were used corresponding to the manufacturer recommendation for resting (low-count) studies. Images were filtered post-reconstruction using a 3D 5th-order Butterworth filter with a cut-off frequency of 0.37 cycles/cm. Images were reconstructed without corrections (NC), with AC and with AC and scatter correction (SC). When applied, AC was based on the CT scan which was coregistered manually to the emission reconstruction using on-line quality assurance tools (*S1*). The uncorrected reconstruction of the myocardial emission activity was visually aligned to be within the CT image of the heart using rigid-body translation and rotation. For the Tc-99m-tracer studies, scatter was estimated using a dual-energy-window approach then filtered (Gaussian FWHM = 3.7 mm) and subtracted from the projection data prior to reconstruction. SC for the Tl-201 studies used a triple-energy-window estimate (TEW) (Gaussian FWHM = 2.0 mm). The energy windows for the Tc-99m-studies were 140.5 keV +/- 10% (photopeak) and 120 keV +/- 5% (scatter). A wider scatter window, similar to that used clinically with conventional cameras, was chosen to reduce noise in the scatter estimate and dilute the contribution of the low-energy tail present in the CZT energy spectrum (*S2*). For Tl-201 studies, the photopeak window was 70 keV -14% + 23% with scatter windows of 100 keV +/- 2.5% and 56 keV +/- 4.5%. The TEW approach was used for Tl-201 due to the presence of down-scatter from the 167 keV emission peak. Scatter corrected projection data were rescaled to correct for the presence of unscattered photons (the low-energy tail) in the lower-energy scatter windows.

Kinetic Modeling

A 1-tissue-compartment-model (CM) was used to analyze the dynamic image series. In this model

$$C_t(t) = K_1\, e^{\left(\frac{-K_1\, t}{DV}\right)} \otimes C_a(t) \qquad \text{Supplemental Eq. 1}$$

where $C_t(t)$ is the tissue concentration of tracer, $C_a(t)$ is the arterial blood concentration, K_1 is the uptake rate constant, $\otimes$ indicates convolution, and DV is the distribution volume (*21*). DV was estimated instead of the clearance rate k_2 to stabilize the parameter fitting; particularly in regions of low flow where separate identification of K_1 and k_2 can be unreliable using the conventional model formulation. $C_a(t)$ was

obtained non-invasively from a volume of interest (VOI) in the left ventricle and corrected for tracer bound to the blood (Supplemental Methods). The time-activity curve, $C_m(t)$, was measured from a myocardial VOI and assumed to be a combination of $C_a(t)$ and $C_t(t)$:

$$C_m(t) = F_a\, C_a(t) + (1 - F_a)\, C_t(t) \qquad \text{Supplemental Eq. 2}$$

F_a is the fraction of arterial blood signal (spill-over) in the myocardial VOI, and $(1\text{-}F_a)$ is the partial-volume recovery coefficient of the tissue signal in the same myocardial VOI.

Tracer Blood Binding

Thallium and sestamibi are known to bind to red blood cells limiting the amount of tracer available to the myocardium for extraction (*18*,*S3*,*S4*). Thus, $C_a(t)$ is better represented by the plasma concentration of tracer instead of the whole blood concentration, as measured by the image-based methods used here. Correction for the plasma to whole blood ratio was applied using a population average function estimated from separate pig experiments. Similar tracer activities, 700 MBq (19 mCi) for Tc99m-tracers and 100 MBq (2.7 mCi) for Tl-201, were injected into 3 pigs and arterial blood samples drawn at 20s intervals for the first 6 min and then at increasing intervals for a duration of 1 hour. Blood samples were immediately centrifuged (Micromax; Thermo Electron Corporation) at 16000 g for 15 sec (*S5*) to separate the red-blood cells from the plasma. The plasma and red blood cells were then decayed and counted in a NaI well-counter to determine the activity. The plasma to whole blood activity concentration ratio (PWR) was averaged over the pigs and the averaged data were fit to Supplemental Equation 3 (*18*). The fitted curve was used to correct the image-derived whole blood concentration curve to a plasma concentration curve.

$$\mathrm{PWR(t)} = A\, e^{\left(-m\,[t+\Delta t]^2\right)} + B\left\{1 - e^{\left(-n\,[t+\Delta t]\right)}\right\} \qquad \text{Supplemental Eq. 3}$$

where t is the time following tracer injection and A, B, n, m and Δt are fitted constants.

SUPPLEMENTAL RESULTS:

All three curves of the plasma to whole blood tracer concentration ratios have a similar shape but with different equilibrium values (Supplemental Fig. 1). The ratio changes rapidly during the first 10min but is near equilibrium by 20min, similar to the results of Iida et al (*18*). The ratio at equilibrium is lowest for Tl-201 and highest for tetrofosmin. The parameters for the curves fit to Eq. 4 are given in Supplemental Table 2.

The FlowQuant™ software also estimates F_a in each of 576 myocardial polar-map sectors. The average F_a was 0.4 for all tracers using NC and AC, but with ACSC dropped to 0.3 ($p<0.02$ vs NC) for the Tc-99m tracers and 0.2 ($p<0.01$) for Tl-201, likely reflecting the added correction for scatter.

SUPPLEMENTAL DISCUSSION:

For AC, we manually aligned a CT scan acquired on a separate camera. Visual alignment of CT scans, while time-consuming, has been used successfully by us and others (*S1*,*S6*,*S7*). However, as the pig's position was not mechanically constrained, small changes in the orientation of the pig between cameras may have occurred that could not be corrected by rigid-body realignment. Automated CT alignment and/or use of a hybrid SPECT/CT camera would improve the logistics of clinical implementation and potentially decrease the likelihood of AC errors due to CT-SPECT misalignment.

SUPPLEMENTAL REFERENCES:

S1. Wells RG, Soueidan K, Vanderwerf K, Ruddy TD. Comparing slow- versus high-speed CT for attenuation correction of cardiac SPECT perfusion studies. *J. Nucl. Cardiol.* 2012; 19:719-726.

S2. Wagenaar DJ. CdTe and CdZnTe semiconductor detectors for nuclear medicine imaging. In: Aarsvold JN and Wernick MN eds. *Emission Tomography: The Fundamentals of PET and SPECT.* San Diego, Elsevier Academic Press, 2004; 269-291.

S3. Marshall RC, Taylor SE, Powers-Risius P, et al. Kinetic analysis of rubidium and thallium as deposited myocardial blood flow tracers in isolated rabbit heart. *Am J Physiol.* 1997; 272(3 Pt 2):H1480-1490.

S4. Marshall RC, Powers-Risius P, Reutter BW, et al. Kinetic analysis of ^{125}I-iodorotenone as a deposited myocardial flow tracer: comparison with 99mTc-sestamibi. *J Nucl Med.* 2001; 42:272-281.

S5. Marshall RC, Powers-Risius P, Reutter BW, et al. Kinetic analysis of ^{18}F-fluorodihydrorotenone as a deposited myocardial flow tracer: comparison to ^{201}Tl. *J Nucl Med*. 2004; 45:1950-1959.

S6. Esteves FP, Galt JR, Folks RD, Verdes L, Garcia EV. Diagnostic performance of lowdose rest/stress Tc-99m tetrofosmin myocardial perfusion SPECT using the 530c CZT camera: Quantitative vs visual analysis. *J Nucl Cardiol.* 2014; 21:158–165.

S7. Herzog BA, Buechel RR, Husmann L, et al. Validation of CT attenuation correction for highspeed myocardial perfusion imaging using a novel cadmium-zinc-telluride detector technique. *J Nucl Med*. 2010; 51:1539-1544.

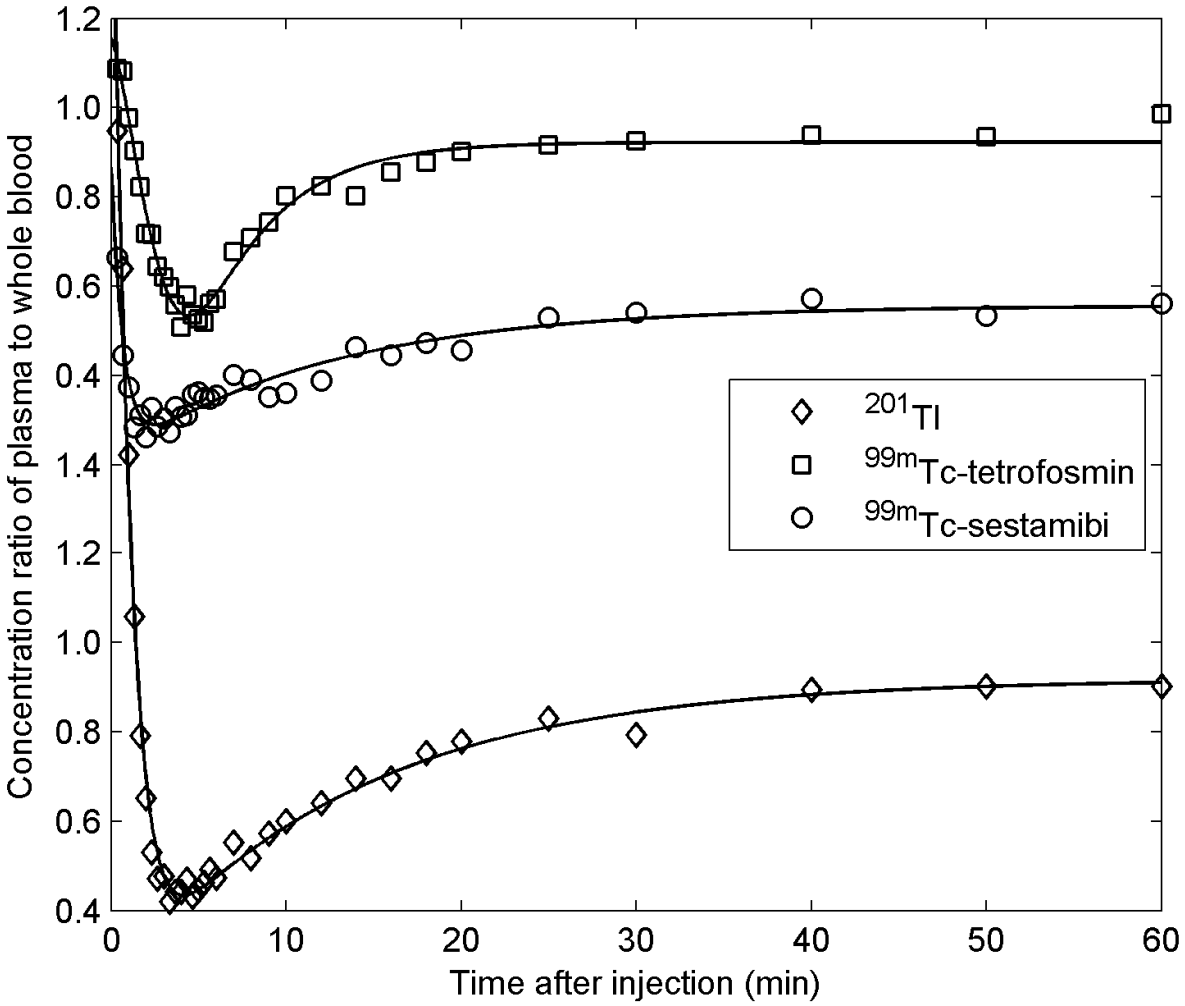

Supplemental Figure 1: Tracer plasma to whole-blood concentration ratios. The average values of the ratio at each time point are shown for each tracer along with the fitted curves. The parameters of the fits to Eq. 4 are given in Supplemental Table 2.

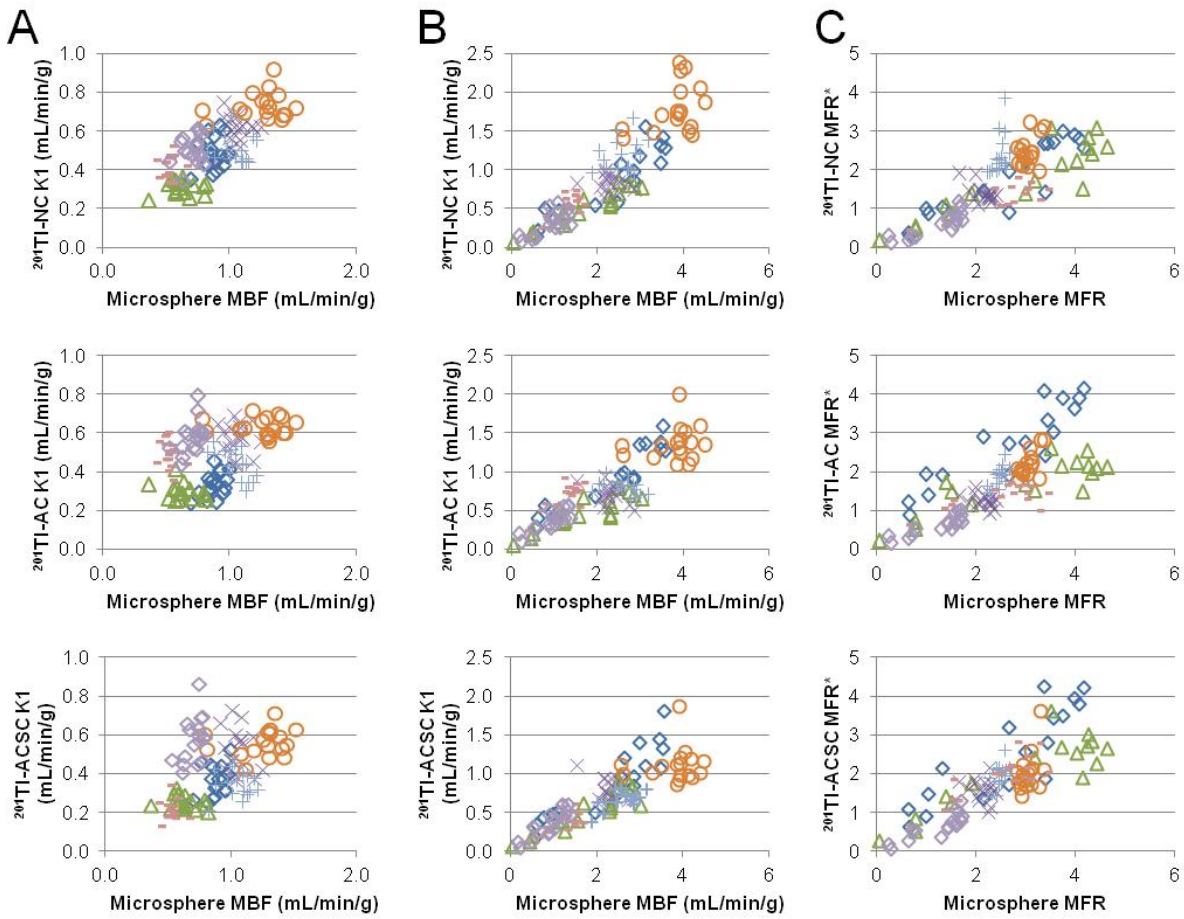

Supplemental Figure 2: 17-segment comparison of Tl-201 K1 estimates to MBF measured with microspheres. Three reconstruction approaches are considered: no corrections (NC), correction for attenuation correction only (AC) and correction for both attenuation and scatter (ACSC). Scatter plots are provided for rest (A), stress (B) and the ratio of stress to rest for K1 (MFR*) compared to microsphere MFR (C).

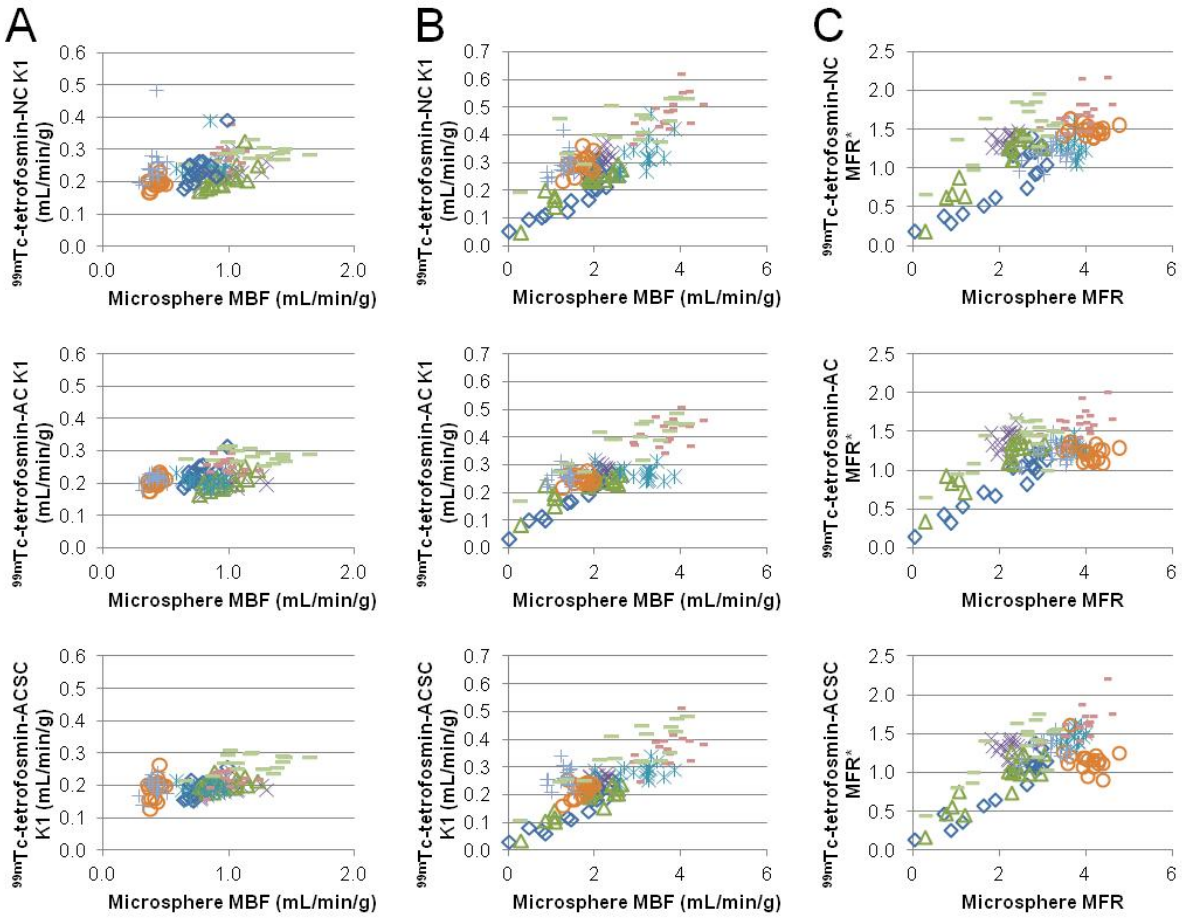

Supplemental Figure 3: 17-segment comparison of Tc-99m-tetrofosmin (Tetro) K1 estimates to MBF measured with microspheres. Three reconstruction approaches are considered: no corrections (NC), correction for attenuation correction only (AC) and correction for both attenuation and scatter (ACSC). Scatter plots are provided for rest (A), stress (B) and the ratio of stress to rest for K1 (MFR*) compared to microsphere MFR (C).

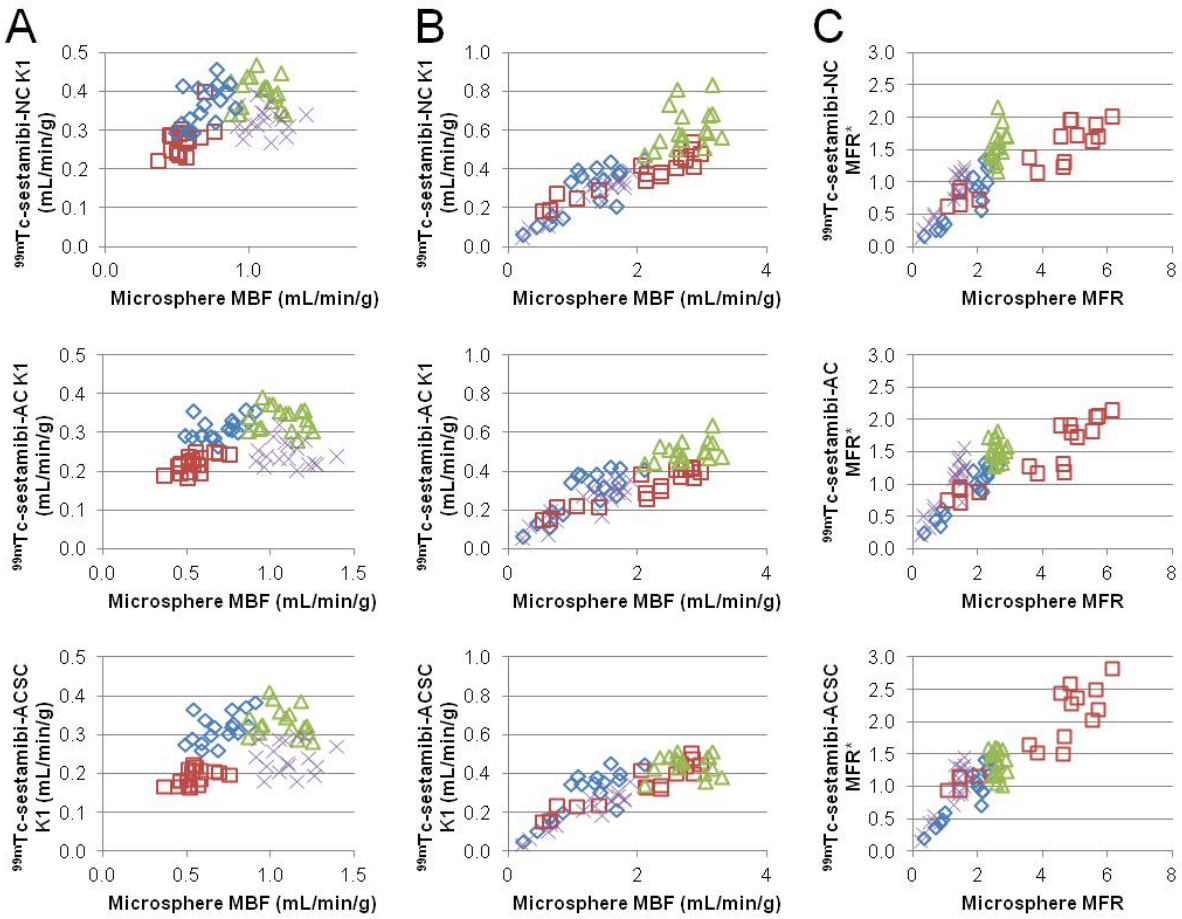

Supplemental Figure 4: 17-segment comparison of Tc-99m-sestamibi (MIBI) K1 estimates to MBF measured with microspheres. Three reconstruction approaches are considered: no corrections (NC), correction for attenuation correction only (AC) and correction for both attenuation and scatter (ACSC). Scatter plots are provided for rest (A), stress (B) and the ratio of stress to rest for K1 (MFR*) compared to microsphere MFR (C).

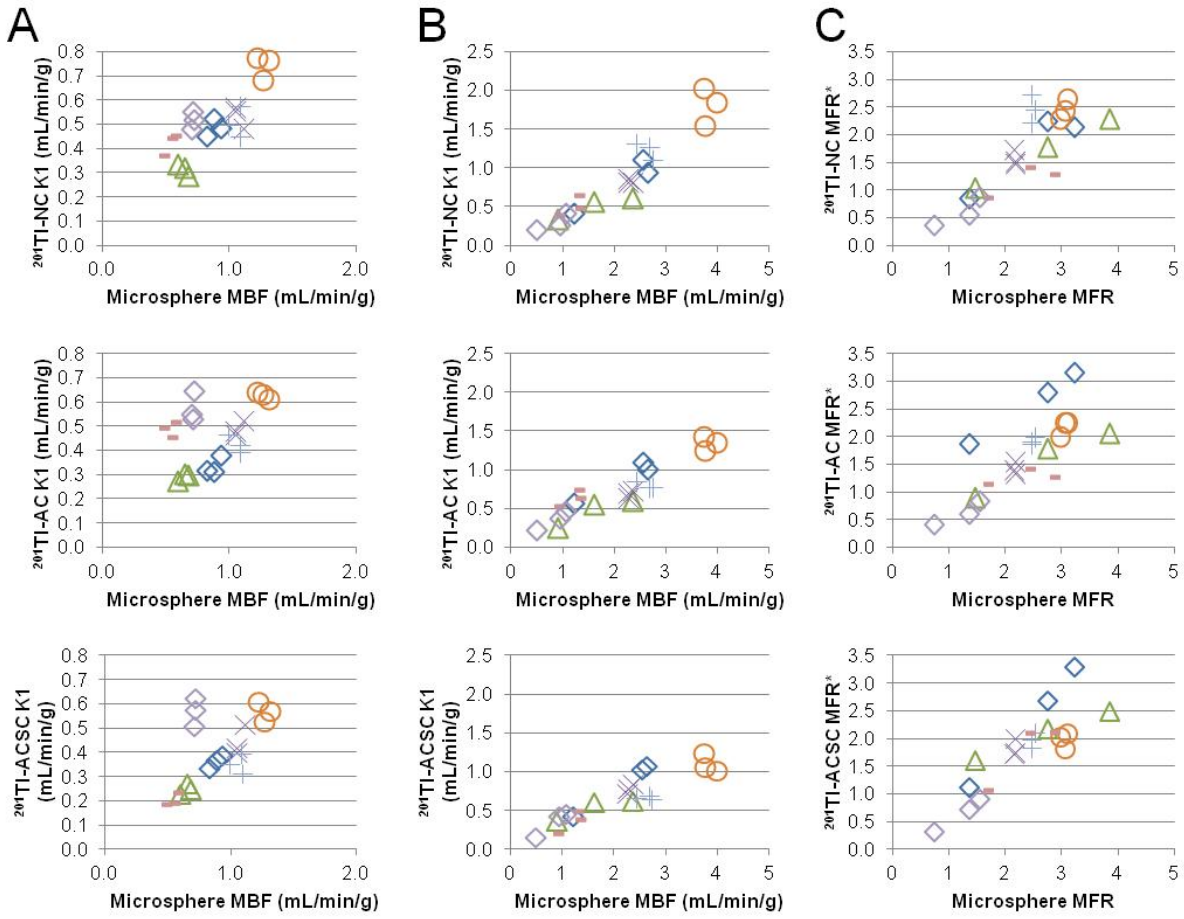

Supplemental Figure 5: 3-segment comparison of Tl-201 K1 estimates to MBF measured with microspheres. Three reconstruction approaches are considered: no corrections (NC), correction for attenuation correction only (AC) and correction for both attenuation and scatter (ACSC). Scatter plots are provided for rest (A), stress (B) and the ratio of stress to rest for K1 (MFR*) compared to microsphere MFR (C).

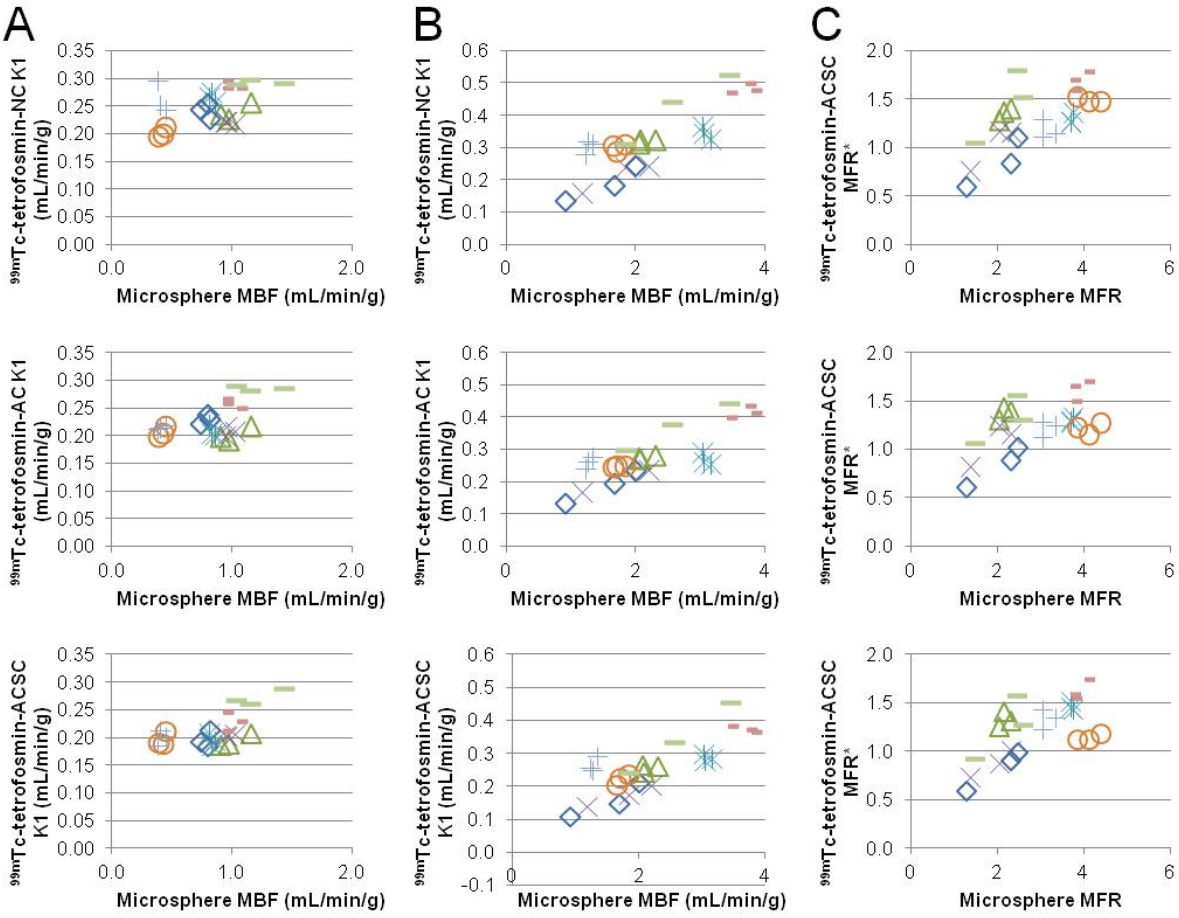

Supplemental Figure 6: 3-segment comparison of Tc-99m-tetrofosmin (Tetro) K1 estimates to MBF measured with microspheres. Three reconstruction approaches are considered: no corrections (NC), correction for attenuation correction only (AC) and correction for both attenuation and scatter (ACSC). Scatter plots are provided for rest (A), stress (B) and the ratio of stress to rest for K1 (MFR*) compared to microsphere MFR (C).

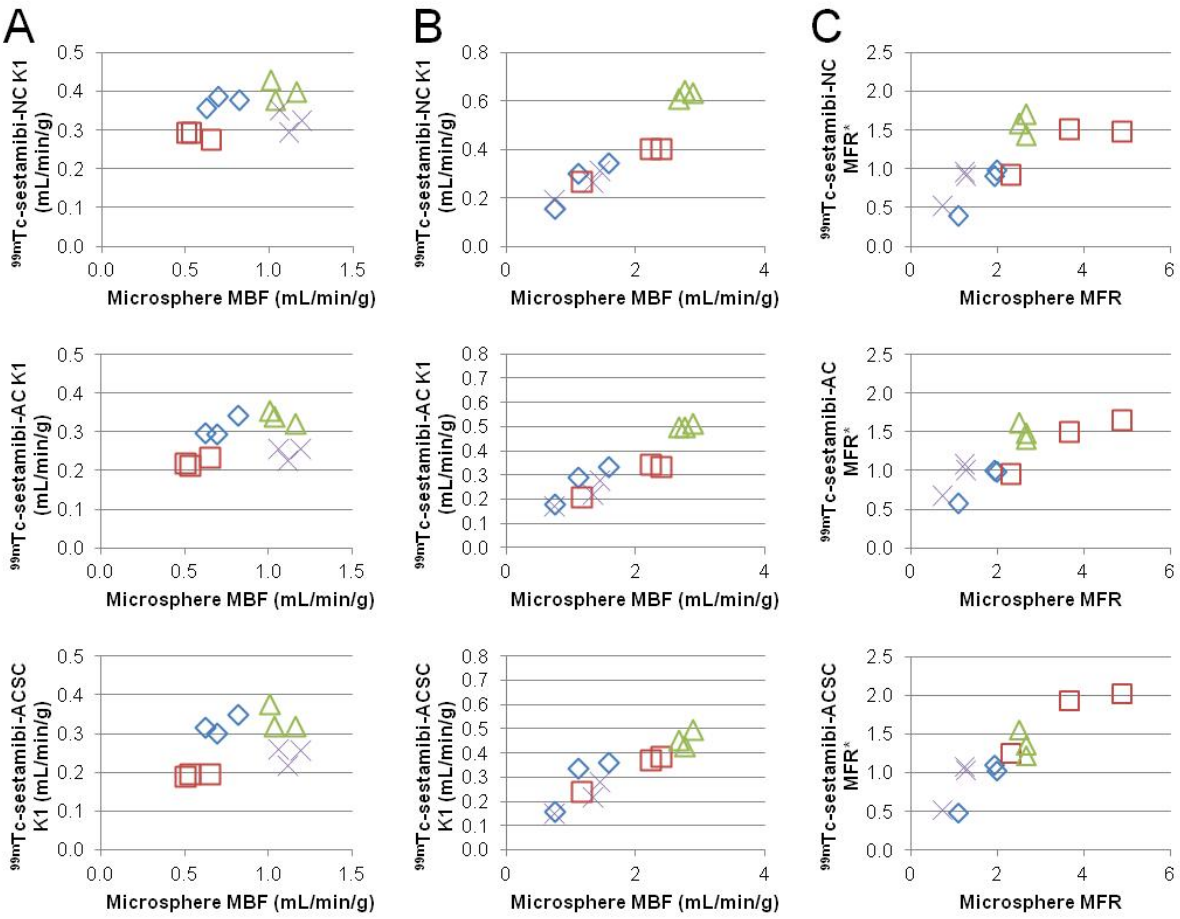

Supplemental Figure 7: 3-segment comparison of Tc-99m-sestamibi (MIBI) K1 estimates to MBF measured with microspheres. Three reconstruction approaches are considered: no corrections (NC), correction for attenuation correction only (AC) and correction for both attenuation and scatter (ACSC). Scatter plots are provided for rest (A), stress (B) and the ratio of stress to rest for K1 (MFR*) compared to microsphere MFR (C).

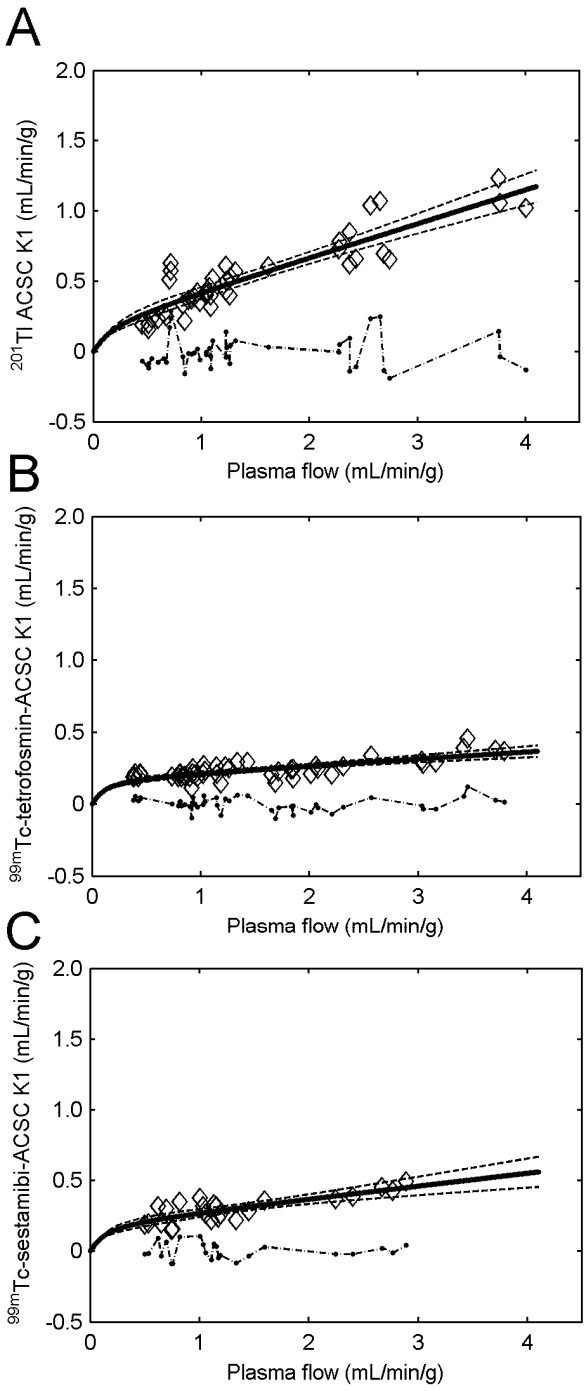

Supplemental Figure 8: 3-segment non-linear least-squares fits of K_1 for rest and stress as a function of microsphere MBF for Tl-201 (ACSC) using a 1-compartment fit (A), tetrofosmin (ACSC) (B) and sestamibi (ACSC) (C). The diamonds show the data points, the solid curve is the fit, the dashed lines show the 95% confidence limit on the fit, and the residuals are shown with the dash-dot curve. Fit parameters and the coefficient of determination (R^2) of the fit are given in Table 3.

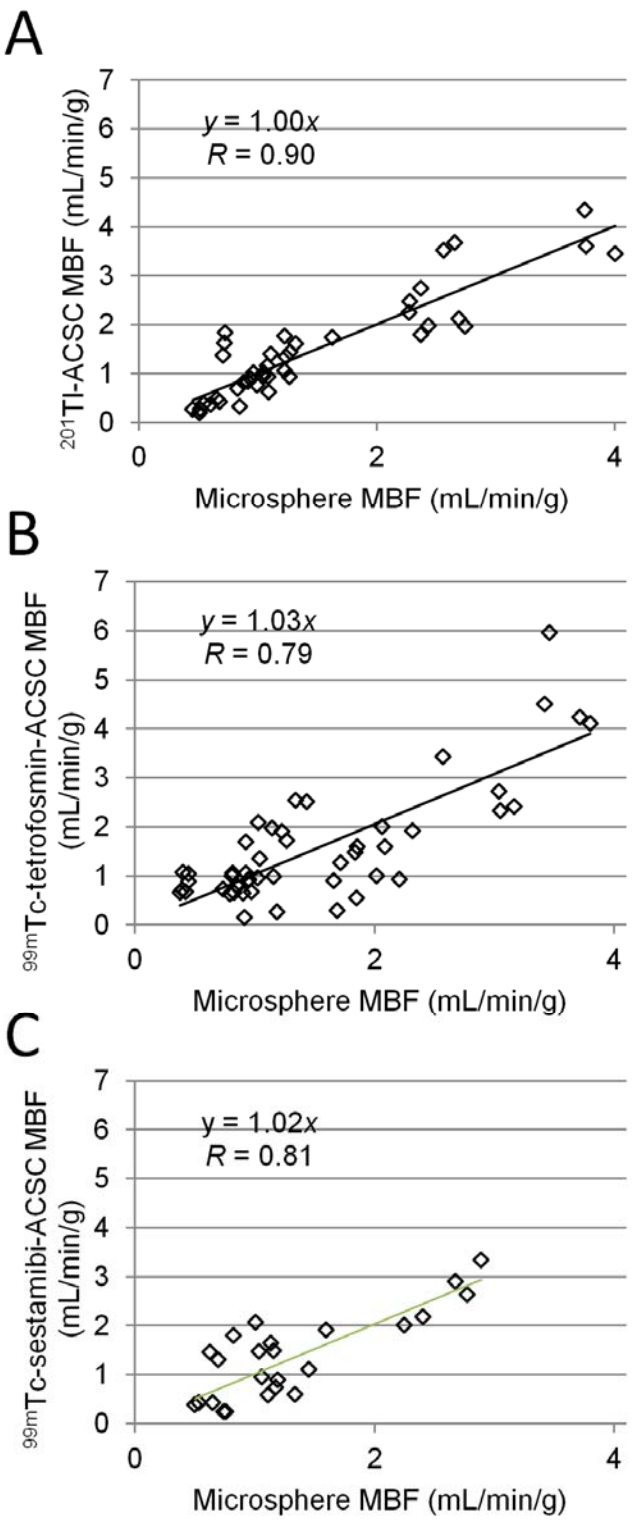

Supplemental Figure 9: 3-segment comparison of microsphere MBF to MBF measured with attenuation and scatter corrected Tl-201 (A), Tc-99m-tetrofosmin (B) and Tc-99m-sestamibi (C). K1 values were converted to MBF using the fitted functions shown in Supplemental Figure 8.

Supplemental Table 1: Pig hemodynamics

	Rest			Stress		
	HR	SBP	DBP	HR	SBP	DBP
Tc99m-sestamibi	85 ± 12	67 ± 21	23 ± 2	83 ± 16	60 ± 19	27 ± 20
Tc99m-tetrofosmin	85 ± 9	69 ± 8	26 ± 7	86 ± 6	63 ± 5	22 ± 6
Tl-201	89 ± 12	64 ± 8	21 ± 8	92 ± 8	61 ± 5	19 ± 11
Aggregate	86 ± 11	66 ± 11	23 ± 7	88 ± 10	61 ± 9	23 ± 11

HR=Heart rate (bpm), SBP=Systolic blood pressure (mm Hg), DBP=Diastolic blood pressure (mm Hg)

Supplemental Table 2: Plasma to whole-blood tracer concentration ratio curves.

Tracer	A	B	m	n	Δt	R^2
Tl-201	96 ± 147	0.65 ± 0.02	0.063 ± 0.015	0.080 ± 0.018	8.0 ± 2.4	0.99
Tetrofosmin	1.18 ± 0.11	1.26 ± 0.01	0.064 ± 0.016	0.24 ± 0.03	2.12 ± 0.89	0.97
Sestamibi	$(1.1 \pm 9.9) \times 10^4$	1.07 ± 0.02	0.044 ± 0.017	0.12 ± 0.05	15.2 ± 7.9	0.90

A, B, m, n, Δt: fitted parameters of Eq. 4. R^2: coefficient of determination of fit

Supplemental Table 3: Average MBF in ischemic and remote territories at stress.

	Average MBF ± SD (mL/min/g)			
	Ischemic Region (Left anterior descending artery territory)			
Tracer	Microspheres	NC	AC	ACSC
Tc-99m-sestamibi	0.89 ± 0.25	0.45 ± 0.22	0.46 ± 0.09	0.45 ± 0.26*
Tc-99m-tetrofosmin	1.32 ± 0.48	0.79 ± 0.85	0.98 ± 1.10	0.71 ± 0.75
Tl-201	0.87 ± 0.29	0.67 ± 0.22	0.83 ± 0.51	0.63 ± 0.37
	Average Remote Region			
Tc-99m-sestamibi	1.69 ± 0.51	1.13 ± 0.36*	1.30 ± 0.39	1.56 ± 0.59
Tc-99m-tetrofosmin	2.30 ± 0.65	2.05 ± 1.98	2.26 ± 1.98	2.09 ± 2.27
Tl-201	1.72 ± 0.70	1.36 ± 0.67	1.78 ± 0.93	1.89 ± 1.12

SD = standard deviation; NC/ AC/ ACSC= no / attenuation / attenuation and scatter correction;

* indicates significant at a Bonferroni corrected p-value of 0.05 / 9 = 0.0056.